Science Advances
AAAS

Supplementary Materials for

Gigantic floating leaves occupy a large surface area at an economical material cost

Finn Box, Alexander Erlich, Jian H. Guan, Chris Thorogood*

*Corresponding author. Email: chris.thorogood@obg.ox.ac.uk

Published 9 February 2022, *Sci. Adv.* **8**, eabg3790 (2022)
DOI: 10.1126/sciadv.abg3790

The PDF file includes:

Other Supplementary Material for this manuscript includes the following:

1 Supplementary details on experimental testing of waterlily leaves

Data were acquired from six specimens of *V. cruziana*, cultivated at the University of Oxford Botanic Garden, over the course of three growing seasons. Data were also acquired from three specimens of *N.* cultivar 'Black Princess' and three specimens *N. lotus*.

Force-displacement curves were obtained from localized, indentation tests. A load was applied to the leaf, above the petiolar attachment, using a mechanical force gage. The resultant deformation was measured by imaging a line drawn across the leaf, using a camera positioned at a known angle to the horizontal and perpendicular to the line, and comparing the relative position of the line to that of the flat, undeformed leaf.

The Young's modulus of both the vasculature, E_{vein} and the lamina E_{lamina} of *Victoria* were measured using an Instron structural testing system. Specifically, E_{vein} and E_{lamina} were measured via compression and tensile tests and found to be $E_{vein} = 0.6\,\mathrm{MPa}$ or $E_{lamina} = 2.7\,\mathrm{MPa}$, respectively. The difference in testing method was a consequence of the geometry of the tissue samples and we suspect that air bubbles/channels in the vasculature matrix are responsible for the low value of Young's modulus of the veins relative to that of the lamina.

Images of the underside of the waterlily leaf were binarized and unwrapped into polar coordinates $(\mathbf{e}_r, \mathbf{e}_\theta)$. For given radial distances, r, from the point of petiolar attachment the image intensity was acquired as a function of azimuthal distance, θ (measured in radians), providing radial scans of the vasculature network (see Fig. S1A). Peaks in the intensity signal corresponded to veins, and the separation between peaks a measure of the angular distance between radial veins, $\lambda = r\theta$ (see Fig. S1B). The measured angular distance between radial veins was found to be approximately constant over six specimens (indicated by the colour of the markers in Fig. S1C), with a mean value of $\lambda = 3.93 \pm 0.54\,\mathrm{cm}$, which gives an approximate measure

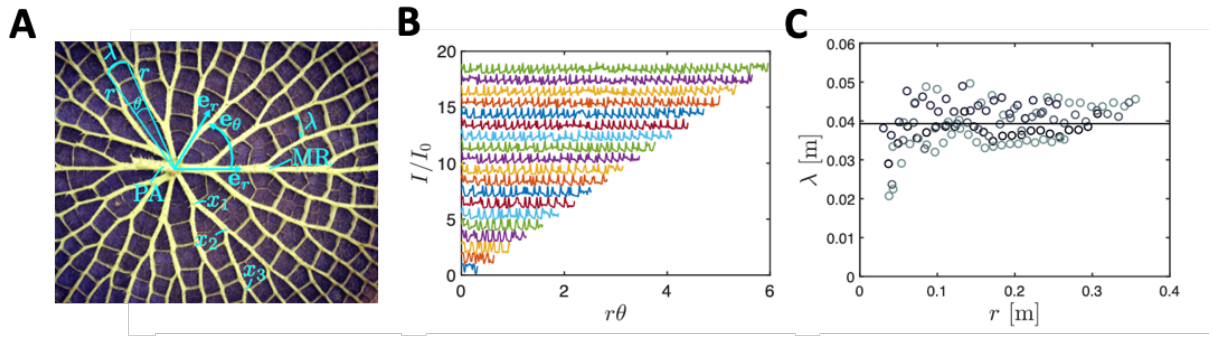

Figure 1: **Angular distance between radial veins**. **(A)** An image of the vasculature showing branching points (x_1, x_2...), the angular distance between radial girders (λ) and the radial coordinate system ($\mathbf{e_r}, \mathbf{e}_\theta$). **(B)** Normalized signal intensity, measured from radial scans of a binarized image of the underside of a *Victoria* lily, as a function of angular distance $\lambda = r\theta$ where peaks correspond to radial veins; consecutive radial scans are offset on the ordinate for visual clarity. **(C)** Wavelength (angular separation distance) between radial veins, $\lambda = r\theta$, measured as a function of radial distance, r, from the petiole attachment (markers) by extracting the average angular separation between peaks in the intensity signals shown in (B). The wavelength is maintained approximately constant throughout the leaf because of regular vein branching; solid line represents the mean value, $\lambda = 3.93 \pm 0.54\,\text{cm}$.

of the length of secondary, orthoradial connective veins (anastomoses).

2 Supplementary details on modelling

Here we outline some details on the implementation of the finite element simulations of water lilies presented in Fig. 3 C–F in the main text. The finite element simulations were performed in Comsol Multiphysics 4.3, specifically in the Plate interface of the Structural Mechanics module. The governing equations of the Plate interface are described in the *Structural Mechanics Module User Guide*, version 4.3, COMSOL, 2012, and shall not be repeated here.

To calibrate our model, we first perform a point indentation test on a circular plate of radius $R_{\text{max}} = 0.41\,\text{m}$, plate thickness $H_L = 0.47\,\text{cm}$, uniform Young's modulus of $E = 2.7\,M\text{Pa}$. An indentation of $\zeta = 0.1\,\text{m}$ is imposed in the simulations in the main text. The buoyancy force per unit area, directed in positive z direction, is calculated as $\rho \cdot g \cdot w$ where ρ is the density of water, g the gravitation constant, and w the displacement of the sheet. We compare

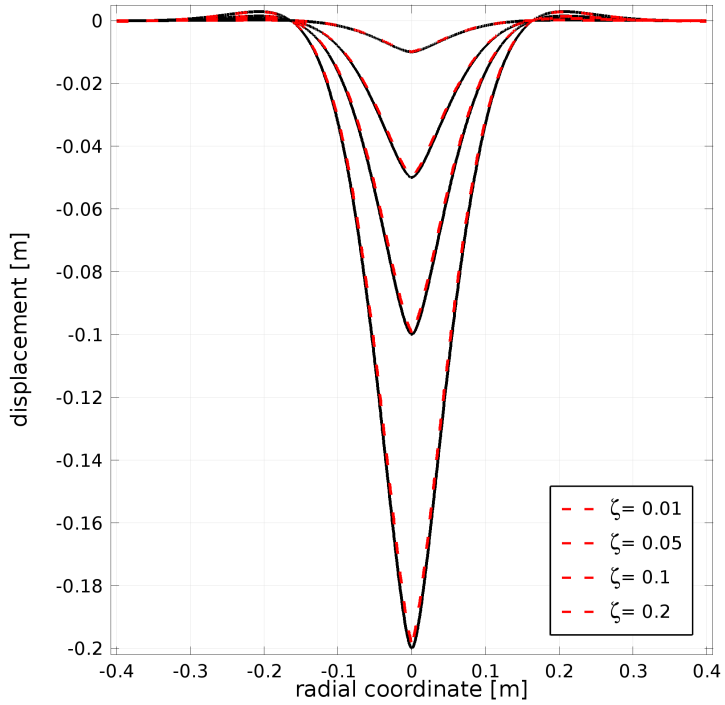

Figure 2: **Comparing finite element solution to exact result from Föppl–von Kármán theory**. The four profiles correspond to different values of the indentation depth ζ, given in metres in the figure legend. The black solid curve shows the exact solution based on Föppl–von Kármán theory derived in reference [7] in the main text. The red dashed curve are solutions of an equivalent setup in the finite elements software Comsol Multiphysics which underlies the simulations in the main text. The solutions show excellent agreement, with the largest relative error for the entire domain being 1.5%.

the result of the COMSOL simulation with an exact analytical solution of the same problem, presented in reference [7] of the main text, Eq. (4.11) of reference [7]. This result was derived in [7] from Föppl–von Kármán theory of thin plates in the limit of low bendability in the case of anxisymmetric deformations. This exact result is compared in Fig. 2 against the Comsol solution, showing excellent agreement for multiple indentation depths ζ.

Next, we demonstrate the convergence of our numerical simulations: As the mesh gets finer, the solution changes less and less, converging to an asymptotic value. Fig. 3 shows the indentation reaction force against the number of triangular elements in the mesh for the

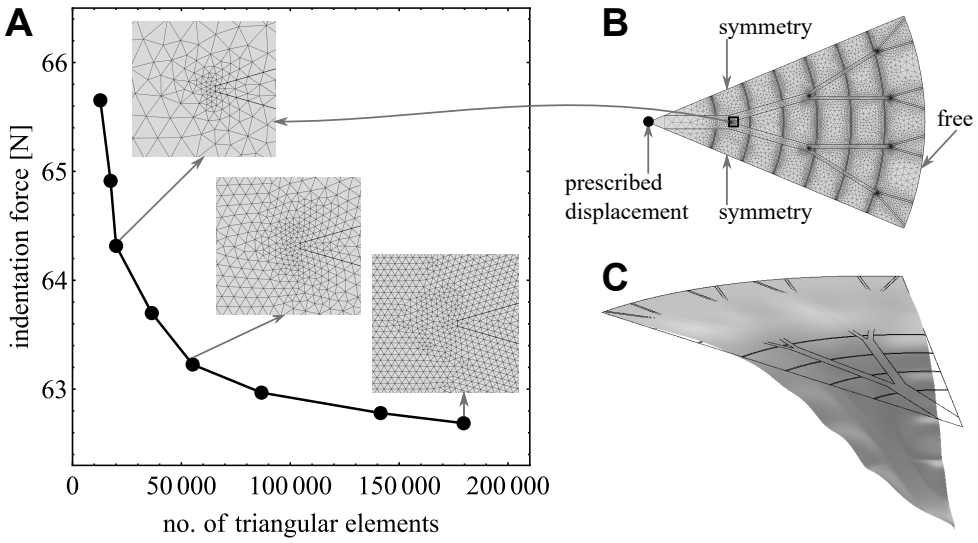

Figure 3: **Convergence of numerical solution.** **(A)** Plot of reaction point force at the center of the disc as a function of an increasingly fine mesh, measured by the number of triangular elements. As the mesh gets finer, the change in solution decreases, converging towards an asymptotic value. **(B)** View of the mesh for the entire solution domain (1/8th of the vasculature) for approx. 20k triangular elements. **(C)** Deformation profile overlaid with outlines of undeformed configuration, showing how the difference in stiffness between lamina and vasculature causes the soft lamina to bulge under buoyancy force.

simulation corresponding to the red line (full model) in Fig. 3D of the main text. The simulation is run for 1/8th of the vasculature, applying symmetry boundary conditions at the two radial cuts. While the 1.57-fold increase in resolution from 12772 to 20019 mesh elements changes the solution of the reaction indentation force by 2.04%, the 1.26-fold increase from 141494 to 179612 mesh elements changes the solution by only 0.15%, showing that the solution appears to be converging to a value below $62.68\,\mathrm{N}$.

Finally, we investigate the effect of the sharp apex of a cone-shaped disk to evaluate to which extent sharp corner affects the solution. In particular, we investigate whether there is a difference if the thickness profile is rounded or sharp, see Fig. 4 . We show in Fig. 4C that as a smoothed cylindrical apex becomes increasingly sharp (parameter R_s going to zero), the solution does not change significantly, reaching an asymptotic value in the restoring force. This

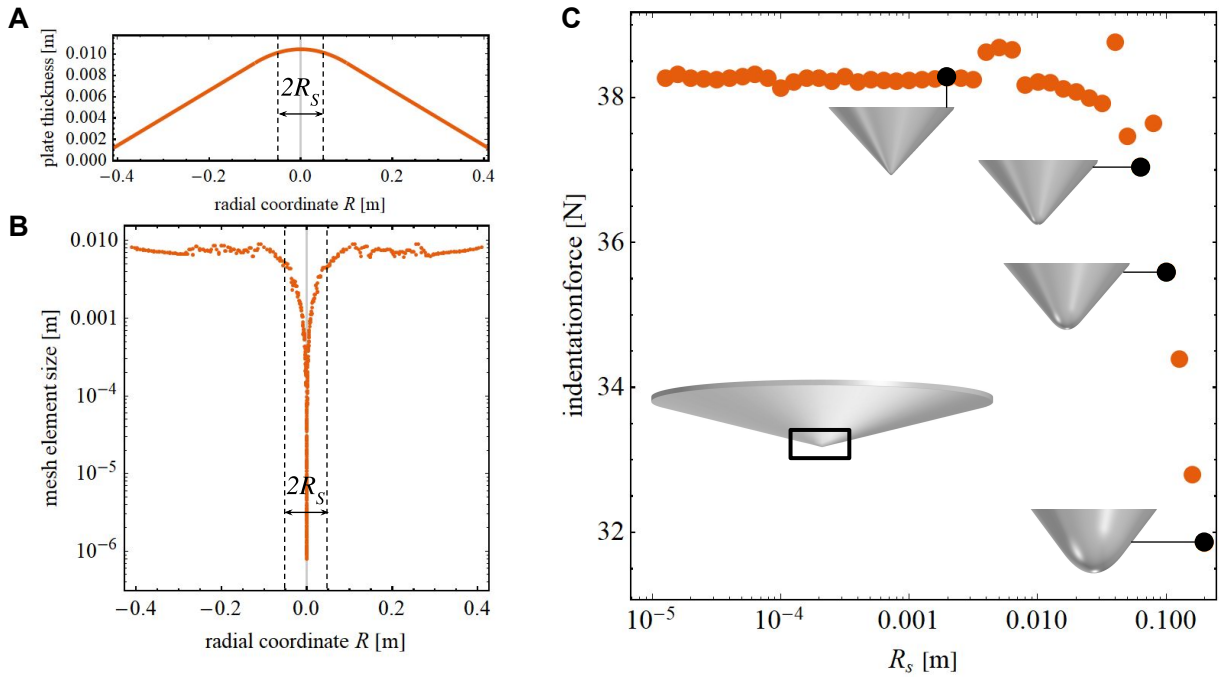

Figure 4: **Convergence of indentation point force as cone tip becomes increasingly sharp.** **(A)** We approximate the cone-shaped thickness profile of the water lily through a linear function if $R > R_s$, and through a smooth approximation (in the form of a parabola with apex at $R = 0$) if $R \leq R_s$. As R_s goes to zero, the cone thickness profile converges to a perfect cone with spiky apex. **(B)** For finite element simulations, the mesh element size Δ is plotted as a function of R for the scenario illustrated in (A), that is $R_s = 0.1$ m. At the indentation point ($R = 0$), the element size Δ is chosen to be extremely small, $\Delta/R_{\text{max}} = 2.49 \cdot 10^{-6}$. This ensures that the indentation point, as well as the rounded tip, are properly resolved. **(C)** As $R_s \to 0$ and the tip becomes increasingly sharp, the indentation reaction force F approaches an asymptotic value of approximately of $F = 38.26$ N, showing that the measurement of indentation force converges. Other parameters are: Undeformed radius $R_{\text{max}} = 0.41$ m, plate thickness at origin $H_0 = 1.175$ cm, thickness at edge of $= 0.1H_0$, uniform Young's modulus of $E = 2.7\,M$Pa, an indentation of $\zeta = 0.1$ m.

result was obtained under the conditions that the indentation point as well as the rounded region are extremely well resolved, see figure caption for details.

Given that for a thickness profile of a sharp cone at the origin, the solution in force response converges towards an asymptotic value, force response values in Fig. 3D result from simulation results based on infinitely sharp cones, eliminating the need to choose an arbitrary value of R_s. The full model, the vasculature only scenario, and the perfect cone scenario in Fig. 3D have sharp cones as the underlying thickness profiles. Furthermore, all four scenarios in Fig. 3D are computed with meshes whose element size Δ is extremely small at the origin, $\Delta/R_{\text{max}} = 2.49 \cdot 10^{-6}$, the same mesh element size as in Fig. 4.

3 Leonardo's rule for vascular branching

Preliminary measurements performed on one waterlily from the collection suggested that the cross-sectional area of veins was conserved across bifurcations. This observation guided our use of the Leonardo's rule in our modelling.

Murray's law is expected when conductance is optimized and Leonardo's rule is expected when mechanical resistance is optimized. To elaborate, it has been shown that when conductance is optimized, Murray's Law holds. However, when vascular tissue functions in both transport and mechanical support, Murray's Law is not obeyed, as for example in conifer wood where hydraulic function is coupled to mechanical support (see McCulloh, K.A., Sperry, J.S. and Adler, F.R., 2004. Murray's law and the hydraulic vs mechanical functioning of wood. Functional Ecology, 18(6), pp.931-938.). Indeed, branching laws usually have (in the notation of Eloy, C., 2011. Leonardo's rule, self-similarity, and wind-induced stresses in trees. Physical review letters, 107(25), p.258101.) the form

$$d^{\Delta} = \sum_{i=1}^{N} d_i^{\Delta} \tag{1}$$

where a mother branch of diameter d splits into N daughter branches of diameter d_i. The Murray exponent is $\Delta = 3$ and Leonardo's exponent is $\Delta = 2$. Murray's Law results in distal-heavy networks that require a larger carbon investment in each newly-added generation, which could compromise the mechanical stability of the plant (Gleason, S.M., Blackman, C.J., Gleason, S.T., McCulloh, K.A., Ocheltree, T.W. and Westoby, M., 2018. Vessel scaling in evergreen angiosperm leaves conforms with Murray's law and area-filling assumptions: implications for plant size, leaf size and cold tolerance. New Phytologist, 218(4), pp.1360-1370.). For this reason, the value of Δ is different from 3 since not only conductance but also biomechanics impose constraints. Indeed, tree branches largely follow area-preserving branching (Leonardo's rule $\Delta = 2$). The above mentioned article by C. Eloy showed that the best design to resist wind-induced fracture in self-similar trees naturally yields Leonardo's rule. Since, as we argue, in the leaves of Amazonian water lilys, mechanical rigidity and stability play an important role in the design of the plant, we chose Leonardo's rule to model the vein size.

4 Supplementary details on load-bearing structures

We designed synthetic structures following the design rules proposed in the main text (see figure 3A-B in the main text). The dimensions of synthetic structures were scaled down by a factor of 0.36. We 3D printed both the vascularized and planar structure using the same amount of liquid photopolymers (and therefore the same volume of material). The structures were held fixed at one end and a custom-built holder (weighing 12g) was attached to the distal edge. To measure deflection profiles under an applied load, different weights were hung from the holder (which ensured that the applied load was applied locally, and uniformly, to the edge of the structures). The deformed strctured was imaged using a camera and the deflection profile was extracted from the images using processing techniques developed in MATLAB.

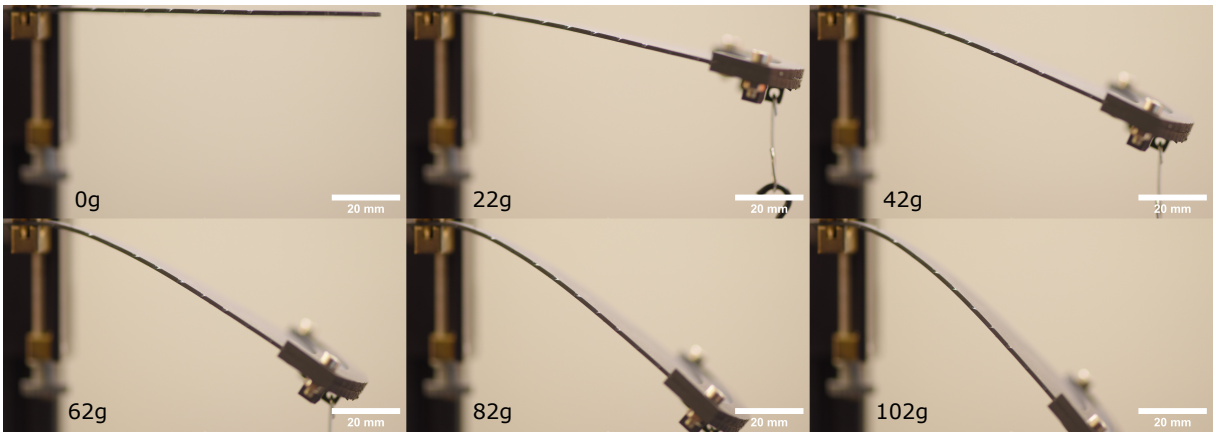

Figure 5: **Synthetic uniform plate.** Image sequence showing the deflection of synthetic structure with uniform thickness under different amounts of load, ranging from 0 to 102g.

5 Data S1. (separate file)

This dataset contains all the experimental and numerical data presented in this study.

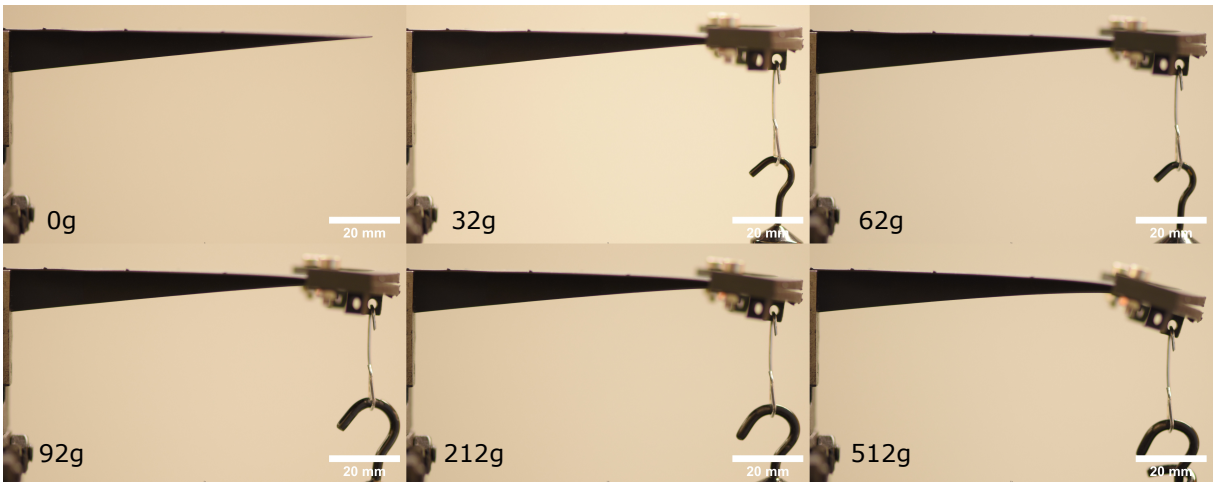

Figure 6: **Synthetic vasculaturized structure.** Image sequence showing the deflection of synthetic vasculaturized structure under different amounts of load, ranging from 0 to 512g.